

Imaging Optically-Thin Hot Spots Near the Black Hole Horizon of Sgr A* at Radio and Near Infrared Wavelengths

Avery E. Broderick* & Abraham Loeb†

Institute for Theory and Computation, Harvard-Smithsonian Center for Astrophysics, 60 Garden St., MS 51, Cambridge, MA 02138, USA

22 August 2018

ABSTRACT

Sub milli-arcsecond astrometry and imaging of the black hole Sgr A* at the Galactic centre may become possible in the near future at infrared and sub-millimetre wavelengths. Motivated by observations of short-term infrared and X-ray variability of Sgr A*, in a previous paper we computed the expected images and light curves, including polarization, associated with an compact emission region orbiting the central black hole. We extend this work, using a more realistic hot-spot model and including the effects of opacity in the underlying accretion flow. We find that at infrared wavelengths the qualitative features identified by our earlier work are present, namely it is possible to extract the black hole mass and spin from spot images and light curves of the observed flux and polarization. At radio wavelengths, disk opacity produces significant departures from the infrared behaviour, but there are still generic signatures of the black hole properties. Detailed comparison of these results with future data can be used to test general relativity and to improve existing models for the accretion flow in the immediate vicinity of the black hole.

Key words: black hole physics, Galaxy: centre, infrared: general, submillimetre, techniques: interferometric, polarization

1 INTRODUCTION

Testing general relativity in a regime where spacetime curvature is large remains one of the primary goals of observational astronomy. Black holes provide a natural target in which to focus these efforts. Nonetheless, due to their extremely compact nature, an unambiguous signature of strong gravity has been elusive so far.

A number of researchers have suggested that imaging an optically-thin background accretion flow could provide a direct test of strong gravity (see, e.g., Falcke et al. 2000; Takahashi 2005, 2004; Broderick & Loeb 2005a). The angular scale of the black hole in the Galactic centre (identified with the radio source Sgr A*) is $5\text{--}10\,\mu\text{s}$, twice as large as the nuclear black hole in M87, and substantially larger than all other candidates. As a result, Sgr A* is the most promising candidate for high resolution imaging. Within the next decade it is expected that a Very Long Baseline Array (VLBA) of sub-millimetre telescopes will exist, providing $20\,\mu\text{s}$ resolution imaging capabilities (Doeleman & Bower 2004; Miyoshi et al. 2004). Thus, theoretical efforts to compute the images of realistic accretion flows is warranted. In

Broderick & Loeb (2005a) it was shown that for a typical accretion model, opacity will be significant at radio wavelengths, substantially altering the shape and visibility of the black hole “shadow” cast by the black hole’s photon capture cross-section.

Multi-wavelength polarization observations of accreting black holes have also been proposed as a method of probing the black hole vicinity (Broderick & Loeb 2005a; Connors et al. 1980; Laor et al. 1990). For optically-thin but geometrically-thick accretion flows, as expected in low luminosity galactic nuclei such as our Galactic centre, it was shown by Broderick & Loeb (2005a) that comparisons of the polarization near and above the optically thick/thin transition frequency is indicative of the black hole spin.

However, observations of near-infrared (NIR) and X-ray flaring of Sgr A* have implied that the inner regions of the accretion flow are nonuniform (Baganoff et al. 2001; Genzel et al. 2003; Goldwurm et al. 2003; Eckart et al. 2004; Ghez et al. 2004). The time scale of the variability, ~ 10 min, is comparable to the period of the innermost stable circular orbit (ISCO), and thus suggestive of an orbiting hot spot. Therefore, it is likely that modeling of Sgr A* images will require the inclusion of variability. In Broderick & Loeb (2005b) it was shown that the images and light curves associated with a hot spot could be used

* E-mail: abroderick@cfa.harvard.edu

† E-mail: aloeb@cfa.harvard.edu

to measure the mass and spin of the black hole. There are additional plans to use the Phase Referenced Imaging and Astrometry (PRIMA) instrument, currently under construction, at the Very Large Telescope (VLT) to obtain sub-milliarcsecond astrometry of these flares (Paumard et al. 2005).

Here we improve upon the calculations of Broderick & Loeb (2005b) by making use of a more realistic hot spot model consisting of a localized population of non-thermal electrons (which are produced, for example, by a magnetic reconnection flare). In addition, we include the effects of disk opacity for a typical radiatively inefficient accretion flow model. The opacity systematically decreases the magnification and polarization fraction, smoothes out the polarization angle light curve, circularizes the motion of the centroid, and symmetrizes the time averaged spot images.

Section 2 presents a summary of the computational methods used and the models for the accretion disk and hot spot. Sections 3 and 5 contain the light curves and centroid paths for NIR and sub-millimetre frequencies, respectively. The effects of opacity are highlighted in section 4. Finally, section 6 summarizes our conclusions.

In what follows, the metric signature is taken to be $(-+++)$, and geometrised unites are used ($G = c = 1$).

2 COMPUTATIONAL METHODS

2.1 Ray Tracing & Radiative Transfer

The method by which the light rays were produced and the radiative transfer performed is discussed at length in Broderick & Blandford (2003) (for which tracing null geodesics is a limiting case) and Broderick & Blandford (2004) (see also Broderick 2005), respectively. As such, only a brief summary is presented here.

Null geodesics are constructed by integrating the equations

$$\frac{dx^\mu}{d\lambda} = f(r)k^\mu \quad \text{and} \quad \frac{dk_\mu}{d\lambda} = -f(r) \left(\frac{1}{2} \frac{\partial k^\nu k_\nu}{\partial x^\mu} \right)_{k_\alpha}, \quad (1)$$

where the partial differentiation is taken holding the covariant components of the wave four-vector, k_μ , constant. The function $f(r)$ is arbitrary (corresponding to the freedom inherent in the affine parameterization, λ) and chosen to be

$$f(r) = r^2 \sqrt{1 - \frac{r_h}{r}}, \quad (2)$$

(where r_h is the horizon radius) in order to regularize the affine parameter near the horizon. Broderick & Blandford (2003) have explicitly demonstrated that this procedure does produce the null geodesics.

Polarized radiative transfer in curved spacetime is most easily performed by integrating the Boltzmann equation (Lindquist 1966; Broderick 2005). In this case, it is the photon distribution function $N_\nu \propto I_\nu/\nu^3$ that is evolved. In the case of polarized radiative transfer, it is possible to define covariant analogues of the Stokes parameters, $\mathbf{N}_\nu = (N_\nu, N_\nu^Q, N_\nu^U, N_\nu^V)$ (Broderick & Blandford 2004). In

$a (M)$	$n_e^0 (\text{cm}^{-3})$	$T_e^0 (K)$	$n_{\text{nth}}^0 (\text{cm}^{-3})$	p_{nth}
0	3×10^7	1.7×10^{11}	8×10^4	-2.9
0.5	3×10^7	1.4×10^{11}	5×10^4	-2.8
0.998	1×10^7	1.5×10^{11}	1×10^5	-2.8

Table 1. The accretion flow parameters associated with equations 4.

terms of these, the radiative transfer equation is

$$\frac{dN_\nu}{d\lambda} = \bar{\mathbf{j}}_\nu - \bar{\alpha}_\nu \mathbf{N}_\nu, \quad (3)$$

where $\bar{\mathbf{j}}_\nu$ and $\bar{\alpha}_\nu$ are emissivity and absorption coefficients (to see how these are related to their standard definitions, see Broderick & Blandford 2004; Lindquist 1966). The two synchrotron emission components considered here involve populations of electrons with a thermal (Yuan et al. 2003) and power-law (Jones & O'Dell 1977) distributions. Because we are primarily concerned with emission at sub-millimetre or shorter wavelengths, Faraday rotation and conversion are unlikely to be important, and are thus neglected.

2.2 Disk Models

We use the same three accretion flow models as described in Broderick & Loeb (2005b). Motivated by Yuan et al. (2003), who showed that the vertically-averaged electron density and temperature are approximately power-laws in radius, we write the thermal electron density, n_e , temperature T_e , and the non-thermal electron density n_{nth} as

$$\begin{aligned} n_e &= n_e^0 \left(\frac{\rho}{M} \right)^{-1.1} \exp(-z^2/2\rho^2) \\ T_e &= T_e^0 \left(\frac{r}{M} \right)^{-0.84} \\ n_{\text{nth}} &= n_{\text{nth}}^0 \left(\frac{\rho}{M} \right)^{p_{\text{nth}}} \exp(-z^2/2\rho^2), \end{aligned} \quad (4)$$

where ρ is the cylindrical radius relative to the black hole spin axis, and p_{nth} is the radial power-law index for the non-thermal electrons. The assumed constants are listed in Table 1. In all models, the non-thermal electrons have a spectral index of 1.25 and a minimum Lorentz factor of 100. The magnetic field strength is set to be a fixed fraction (30%) of equipartition relative to the protons. As suggested by recent general-relativistic magnetohydrodynamic simulations, the field is taken to be toroidal (De Villiers et al. 2003). The accreting gas is assumed to be in free fall inside of the ISCO ($6M$, $4.233M$ and $1.237M$ for $a = 0$, 0.5 and 0.998 , respectively), and in Keplerian rotation otherwise. In all cases the disk angular momentum was aligned with the spin of the black hole.

2.3 Hot Spot Model

The hot spot is modeled by an overdensity of non-thermal electrons centered at a point orbiting at the Keplerian velocity with a Gaussian profile as measured in the comoving frame:

$$n_S = n_S^0 \exp \left[-\frac{\Delta r^\mu \Delta r_\mu + (u_S^\mu \Delta r_\mu)^2}{2R_S^2} \right] \quad (5)$$

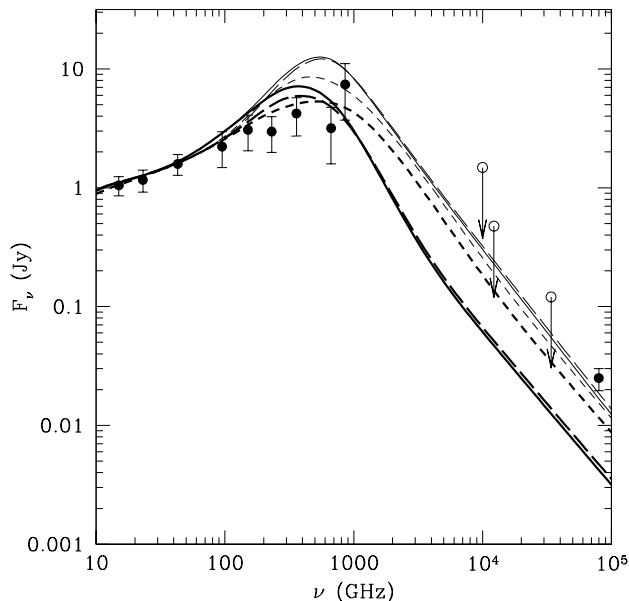


Figure 1. The spectral flux for the non-rotating ($a = 0$, solid), moderately rotating ($a = 0.5$, long-dashed), and maximally rotating ($a = 0.998$, short-dashed) Sgr A* disk models as viewed from 45° degrees above the equatorial plane. The thick lines correspond to the quiescent disk emission and the thin lines correspond to the peak flare flux for a spot located at an orbital radius of $6M$. The data points are taken from the compilation by Yuan et al. (2004).

where $\Delta r^\mu \equiv r^\mu - r_S^\mu$ is the displacement from the spot centre (located at r_S^μ), u_S^μ is the spot four-velocity, n_S^0 is the spot central number density, and R_S is a measure of the spot radius. So that our results may be easily compared with Broderick & Loeb (2005b), we used $R_S = 1.5M$. The spot central number density was chosen to roughly reproduce the observed peak NIR flare flux. As suggested by coincident NIR–X-ray observations, the hot spot spectral index was assumed to be 1.3 (Eckart et al. 2004), and the minimum Lorentz factor was assumed to be 100. Such a situation may arise, e.g., in the case of reconnection event similar to a solar flare. The spectrum of the disk and our canonical flare model (at an orbital radius of $6M$, viewed from 45° above the equatorial plane) are shown in Figure 1. Below 100 GHz the disk photosphere extends beyond the hot spot, quenching its contribution to the over all flux. Above 100 GHz the hot spot becomes increasingly visible, reaching a maximum near 500 GHz.

For the Galactic centre, the orbital time scale near the ISCO are between 5 min and 30 min for orbits around maximally and non-rotating black holes, respectively. The viability of a hot-spot model for the flaring in Sgr A* requires that the synchrotron cooling time scale be large in comparison to the orbital period. Since the emission at a frequency ν is dominated by electrons with Lorentz factor $\gamma_e = \sqrt{\nu/\nu_B}$, where ν_B is the classical electron cyclotron frequency, the cooling time of a flare as observed at ν is

$$\tau_c \simeq 10^2 \left(\frac{\nu}{10^3 \text{ GHz}} \right)^{-1/2} \left(\frac{B}{30 \text{ G}} \right)^{-3/2} \text{ min} . \quad (6)$$

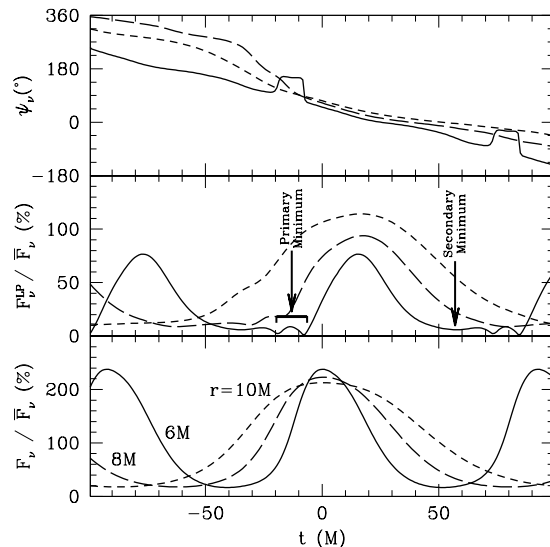


Figure 2. The background subtracted total and polarized flux (bottom and middle panels, respectively) normalized by the average background subtracted total flux in the optically-thin regime as functions of time for spot circular orbits at $6M$ (solid), $8M$ (long-dash) and $10M$ (short-dash) around a Schwarzschild black hole, viewed from 45° above the equatorial plane. The top panel shows the polarization angle, ψ . The time axis is set so that a single orbital period of the $10M$ case is shown. For a black hole mass of $4 \times 10^6 M_\odot$ (as in Sgr A*), the time unit is $M = 20$ s.

For the frequencies considered here this ranges from many hours (in the sub-millimeter regime) to tens of minutes (in the NIR). Hence, the highest frequencies at which a substantial portion of the orbit is likely to be visible are those in the NIR.

In order to concentrate upon the hot spot emission, all following plots are of *background subtracted* quantities, i.e., the quiescent disk emission has been removed.

3 NEAR INFRARED

As shown in Broderick & Loeb (2005a), above $\sim 10^3$ GHz, the accretion flow is optically thin everywhere. As a result, at NIR frequencies the emission from the hot spot is unadulterated. For this reason we discuss the light curves and centroid paths in the NIR first. Note that due to the fact that the spectra above $\sim 10^3$ GHz has constant spectral index, the results of this section apply to all wavelengths above the optically thick/thin transition. These may be directly compared with the results of Broderick & Loeb (2005b).

3.1 Light Curves

As in Broderick & Loeb (2005b), the primary distinction between hot spots located at different radii is the time scale of variability in the total flux. This can be seen explicitly in the lower panel of Figure 2 in which the magnification of the *hot spot emission* is shown as a function of time. This is evident in the polarized flux variability as well (middle panel). It

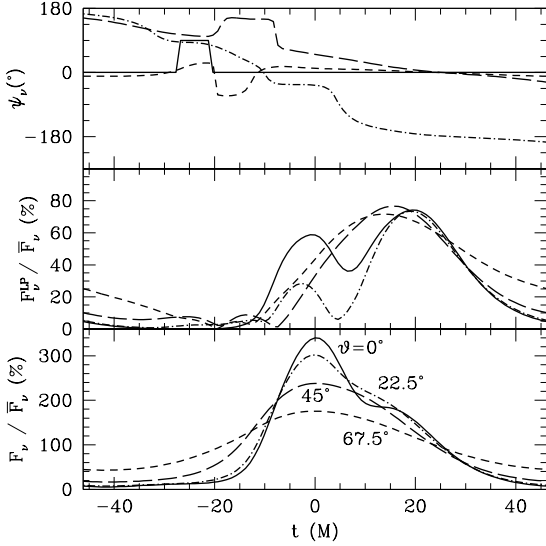


Figure 3. The background subtracted total and polarized flux (bottom and middle panels, respectively) normalized by the average background subtracted total flux in the optically-thin regime as functions of time for a spot orbit at $6M$ around a Schwarzschild black hole viewed from 0° (solid), 22.5° (dash-dot), 45° (long-dash) and 67.5° (short-dash) above the equatorial plane. The polarization angle, ψ , is shown in the top panel. For a black hole mass of $4 \times 10^6 M_\odot$ (as in Sgr A*), the time unit is $M = 20$ s.

should be noted that the polarization variability will be different from that found in Broderick & Loeb (2005b) owing to the difference in the polarized emission models (the one utilized here being the more physically motivated). Nonetheless, the generic features of a primary minimum caused by the development of the secondary hot-spot image (immediately preceding maximum unpolarized magnification) and a weaker secondary minimum caused by the development of a tertiary image (following the maximum unpolarized magnification by $60M$) exist. In this case the polarization angle is punctuated by rapid rotations ($\sim 90^\circ$) at the primary minimum, and uneventful otherwise, rotating as expected for a toroidal field.

Characteristically, the peak polarized flux follows the peak magnification. In the canonical case of an spot orbital radius of $6M$ viewed from 45° above the orbital plane, this corresponds to a delay of approximately 5 min in the context of the Galactic centre.

Again, variations in viewing inclination, ϑ , produces similar effects as those reported in Broderick & Loeb (2005b), the primary distinction being the total magnification. There are structural changes in the polarized flux, indicative of the prominence of the primary and secondary hot-spot images. Unlike Broderick & Loeb (2005b), in the edge-on view ($\vartheta = 0^\circ$), strong gravitational lensing produces a polarization component orthogonal to dominant polarization, leading to a rapid rotation in polarization angle preceding peak magnification by approximately a quarter-phase.

The manifestation of black hole spin in the light curves is shown in Figure 4. As in Broderick & Loeb (2005b), the differences among the magnification light curves is small in comparison to those associated with variations of the orbital

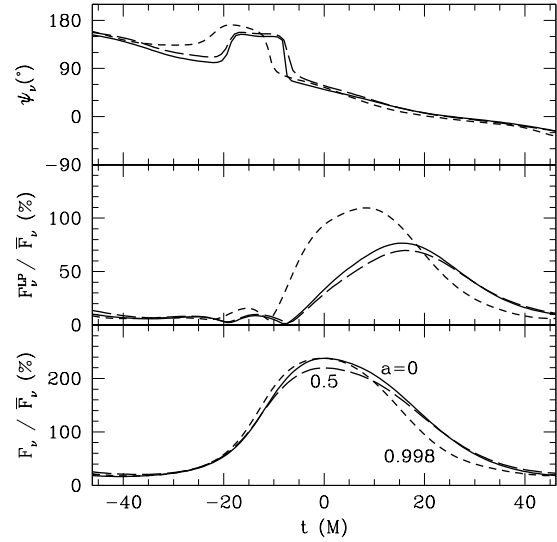


Figure 4. The background subtracted total and polarized flux (bottom and middle panels, respectively) normalized by the average background subtracted total flux in the optically-thin regime as functions of time for a spot orbit at $6M$ around a Kerr black hole with $a = 0$ (solid), $a = 0.5$ (long-dash) and $a = 0.998$ (short-dash) viewed from 45° above the equatorial plane. The polarization angle, ψ , is shown in the top panel. The time axis is set so that a single orbital period of the $a = 0$ case is shown. For a black hole mass of $4 \times 10^6 M_\odot$ (as in Sgr A*), the time unit is $M = 20$ s.

parameters. While the secondary minimum of the polarization does vary significantly with spin, in the total flux this is difficult to observe.

However, the primary distinction between different spins is likely to be the variations in the radius of the ISCO, and thus the typical periods. Figure 5 shows the magnification and polarization light curves for a spot viewed from 45° above the equatorial plane located at the prograde ISCO for various dimensionless spin parameters (normalized by M), namely $6M$, $4.233M$ and $1.237M$ for $a = 0$, 0.5 and 0.998 , respectively. Because the orbital timescales vary by nearly an order of magnitude between $a = 0$ and $a = 0.998$, these are plotted as functions of *orbital phase*. Rapid rotation substantially reduces the maximum polarized flux, primarily due to the enhanced gravitational lensing associated with the compactness of the orbit. However, as mentioned in Broderick & Loeb (2005b), and alluded to above, the most significant discriminator is likely to be the event time scale.

3.2 Centroid Paths

The PRIMA instrument at the VLT is expected to provide sub-milli-arcsecond astrometry, thus enabling high resolution measurements of the the infrared image centroid for Sgr A* and in turn constrain the accretion flow and black hole parameters. Because the location of the image centroids will be dominated by the brightest features, subtracting the background accretion flow emission is necessary to isolate the location of the hot spot during a flare. However, intrinsic variability in the source and/or the presence of multiple hot spots may introduce substantial systematic errors into

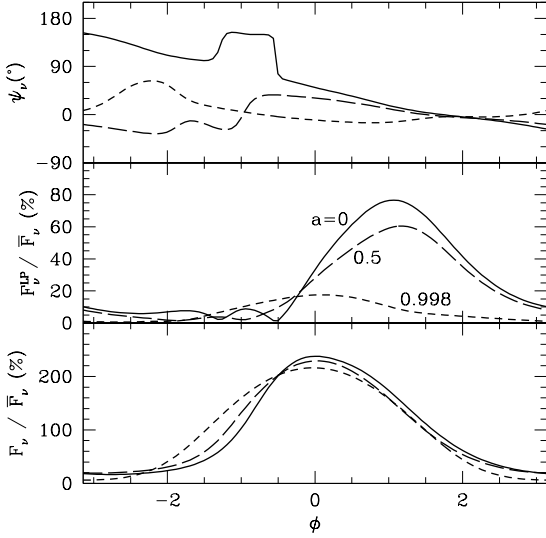


Figure 5. The background subtracted total and polarized flux (bottom and middle panels, respectively) normalized by the average *background subtracted* total flux in the optically-thin regime as functions of phase for spot orbits at the prograde ISCO around a Kerr black hole with $a = 0$ (solid), $a = 0.5$ (long-dash) and $a = 0.998$ (short-dash) viewed from 45° above the equatorial plane. The polarization angle, ψ , is shown in the top panel. The time axis is set so that a single orbital period of the $a = 0$ case is shown. For a black hole mass of $4 \times 10^6 M_\odot$ (as in Sgr A*), the time unit is $M = 20$ s.

this process. Nonetheless, in order to clearly remove the uncertainty associated with the accretion disk model, in computing all of the centroid positions below we have used the *background subtracted* images. These may be generated using the centroids of the total emission if the quiescent centroid position and intensity are known:

$$\overline{\mathbf{X}}_S(t) = \frac{F(t)\overline{\mathbf{X}}(t) - F_{BG}\overline{\mathbf{X}}_{BG}}{F(t) - F_{BG}}, \quad (7)$$

where $\overline{\mathbf{X}}_S(t)$ is the location of the spot centroid, $\overline{\mathbf{X}}(t)$ and $F(t)$ are the location of the total image centroid and the total observed flux, and $\overline{\mathbf{X}}_{BG}$ and F_{BG} are the background (disk) image centroid and flux.

While gravitational lensing and relativistic aberration distort the centroid path, it is nevertheless possible to determine the orbital radius (Figure 6) and inclination (Figure 7). Combined with the orbital period at an orbital radius r_S (in units of M),

$$P = 2\pi M \left(r_S^{3/2} - a \right), \quad (8)$$

(where positive a corresponds to prograde orbits) determined, e.g., by the magnification light curve, this provides a direct measurement of the spin.

Figures 8 and 9 present the effects of black hole spin upon the centroid paths. In Figure 8 the hot spot is located at $6M$ and viewed from 45° above the orbital plane. In this case a moderate increase in the orbital velocity with spin leads to an enhancement of the relativistic beaming, shifting the centroid path towards the approaching side (left). In Figure 9 the hot spot is located at the prograde ISCO for

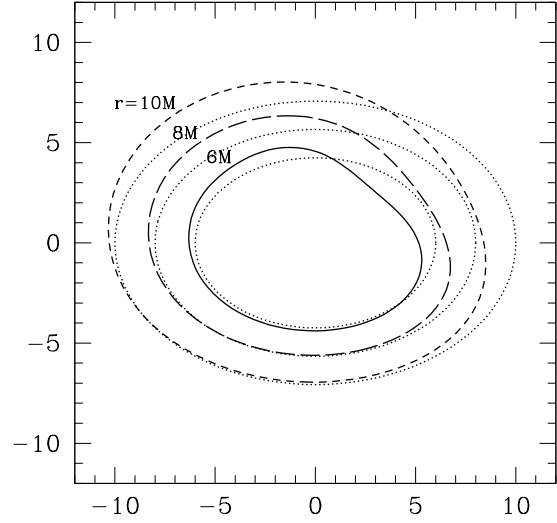


Figure 6. The paths of the background subtracted intensity centroid in the optically-thin regime for circular spot orbits around a Schwarzschild black hole viewed from 45° above the orbital plane with radii $6M$ (solid), $8M$ (long-dash) and $10M$ (short dash). For reference, a circle inclined at 45° is also shown by the dotted lines for each radius. Axes are labeled in units of M (corresponding to an angular scale of roughly $5 \mu\text{as}$ for Sgr A*).

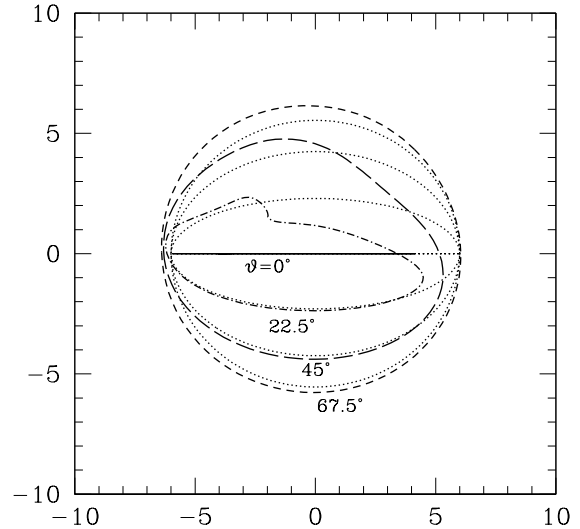


Figure 7. The paths of the background subtracted intensity centroid in the optically-thin regime for circular spot orbits around a Schwarzschild black hole with radius $6M$ viewed from 0° (solid), 22.5° (dash-dot), 45° (long-dash) and 67.5° (short-dash) above the orbital plane. For reference, a circles inclined at each angle are shown by the dotted lines. Axes are labeled in units of M (corresponding to an angular scale of roughly $5 \mu\text{as}$ for Sgr A*).

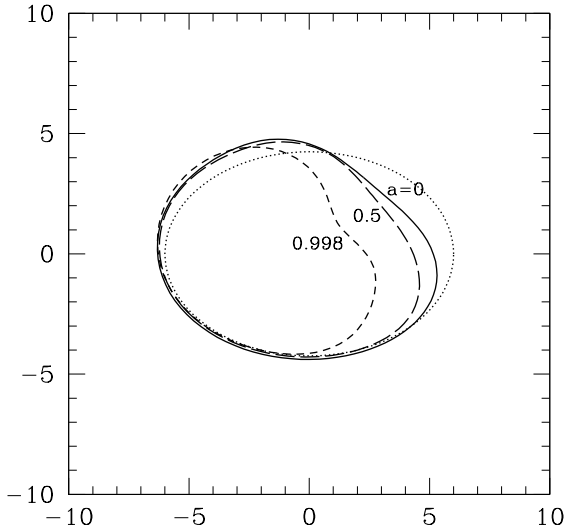


Figure 8. The paths of the background subtracted intensity centroid in the optically-thin regime for circular spot orbits with radius $6M$ in the equatorial plane around a Kerr black hole viewed from 45° above the orbital plane for $a = 0$ (solid), $a = 0.5$ (long-dash) and $a = 0.998$ (short-dash). For reference, a circle inclined at 45° is also shown by the dotted line. Axes are labeled in units of M (corresponding to an angular scale of roughly $5\mu\text{as}$ for Sgr A*).

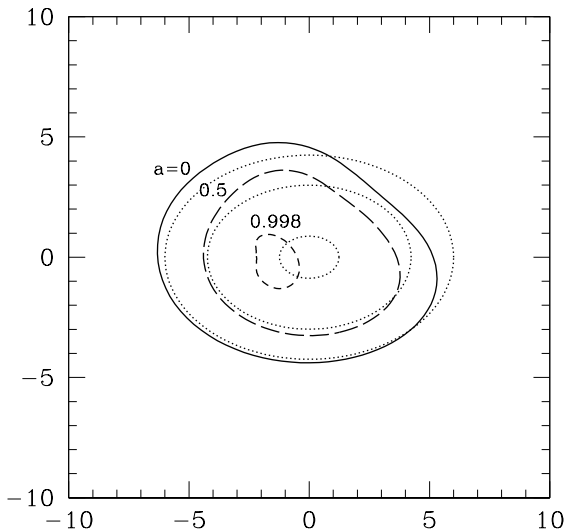


Figure 9. The paths of the background subtracted intensity centroid in the optically-thin regime for circular spot orbits around a Kerr black hole viewed from 45° above the orbital plane at the prograde ISCO for $a = 0$ (solid), $a = 0.5$ (long-dash) and $a = 0.998$ (short-dash). For reference, a circle inclined at 45° is also shown by the dotted lines for spin. Axes are labeled in units of M (corresponding to an angular scale of roughly $5\mu\text{as}$ for Sgr A*).

each black hole spin, again viewed from 45° above the orbital plane. Here the centroid path at high spin, where the ISCO is close to the horizon, is substantially offset. However, in the case of moderate spin, the generic dependence upon radius seen in Figure 6 is dominant.

4 GENERIC EFFECTS OF OPACITY

While in the NIR the disk opacity to synchrotron self-absorption is negligible, this is not the case at sub-millimeter wavelengths, at which the accretion flow is only beginning to be optically thin. As discussed in Broderick & Loeb (2005a), the accretion flow opacity is not symmetric between the two sides of the disk, and is enhanced by the Doppler effect on the approaching side of the disk. As a result, the light curves and centroid paths presented in the previous section for the NIR can be substantially modified for frequencies near the optically thick/thin transition. For the purpose of highlighting the generic effects of opacity, and the utility of high-resolution multi-wavelength flare observations, we present next a comparison of the light curves and centroid paths for NIR and radio frequencies.

4.1 Time Averaged Images

The effects of asymmetric opacity are readily apparent in the orbit-averaged images, shown in Figure 10 for the canonical hot-spot model for the three disk models discussed in Section 2.2, as observed at 230 GHz, 350 GHz and in the NIR. In the NIR both the direct and secondary images are clearly visible, corresponding to the larger and smaller rings, respectively. Less visible are the tertiary images, which produce the very thin ring directly inside that associated with the secondary images. In addition, as expected from the Doppler shift and relativistic beaming, the approaching portion of the hot-spot orbit (left side) appears considerably brighter than the receding portion of the spot orbit (right side). At radio frequencies the secondary image is substantially less visible and the brightness contrast between the approaching and receding portions of the hot-spot orbit decreases with decreasing frequency. This is a direct result of the increased opacity in the approaching portion of the disk (also on the left side). As mentioned in Broderick & Loeb (2005b), in the limit of a thermal spectrum the orbit-averaged images are symmetric, and thus it is not surprising that increased opacity results in more symmetric images.

Also shown in Figure 10 is the degree and orientation of the polarized flux. In all cases this is dominated by the approaching portion of the orbit. In the NIR, a second polarization component is present due to the secondary image. This is substantially suppressed at radio wavelengths, and thus the strong swings in polarization angle are not expected in the radio. Finally, the degree of polarization is also expected to decrease as a result of the decrease in the brightness asymmetry mentioned before.

4.2 Light Curves

Figures 11–13 shown the magnification and polarized flux light curves in the radio and NIR for a hot-spot orbiting an $a = 0$, 0.5 and 0.998 black hole, respectively. The primary

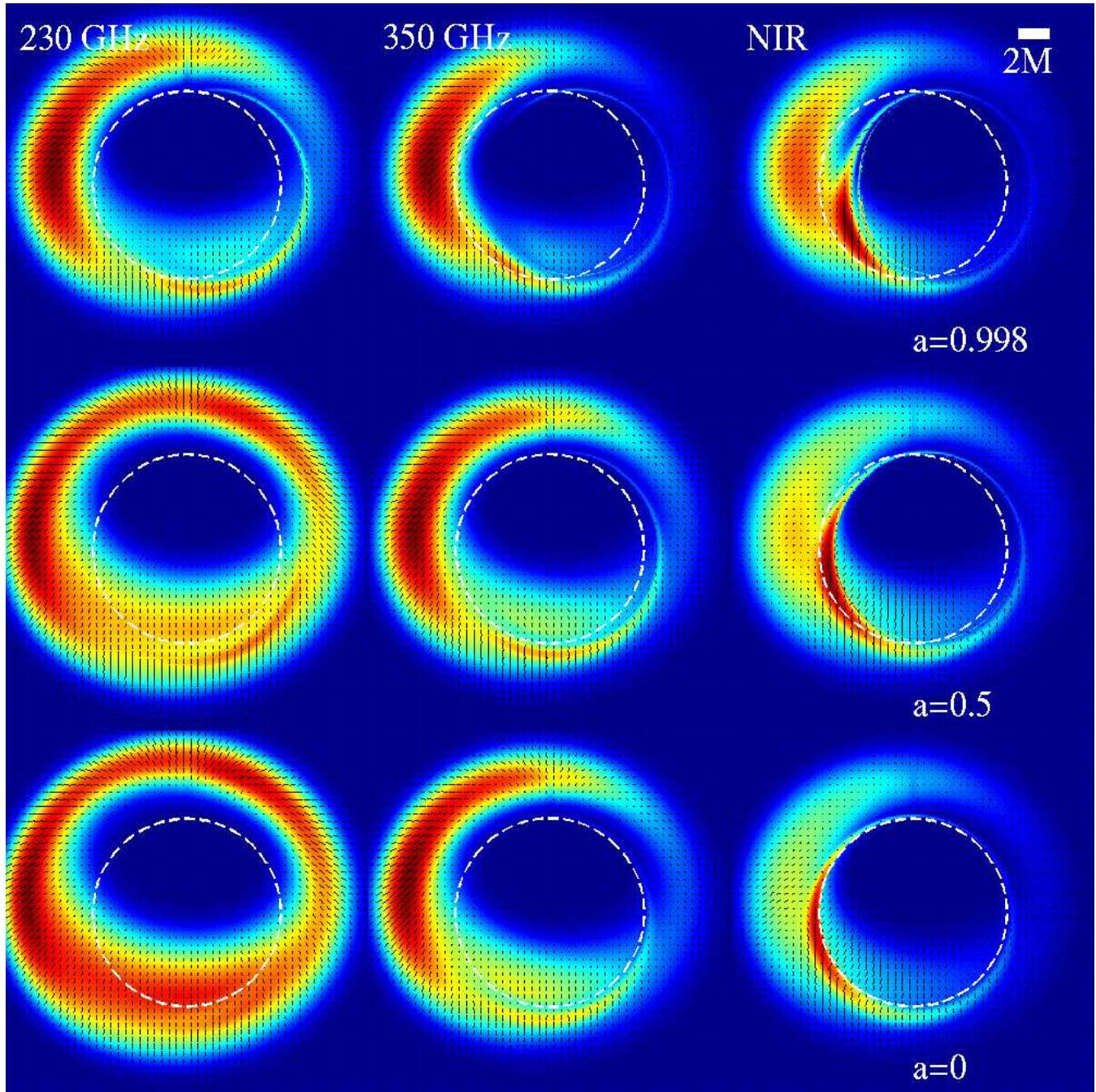


Figure 10. Comparison of the orbit-averaged, disk-subtracted images of a spot for two radio frequencies (at which opacity is important) and in the infrared (at which the disk is transparent). For reference, the photon-capture cross section for a Schwarzschild black hole is shown by the dashed white line.

distinction between the different observing wavelengths is in the degree of polarization, decreasing by roughly an order of magnitude from the NIR to 230 GHz. In addition, as expected from the images, the polarization angle light curve is progressively smoothed as the observing wavelength increases. It should also be noted that the secondary minimum in the polarization, also resulting from the development of tertiary images, is significantly less visible in the radio.

4.3 Centroid Paths

The centroid paths for different observing frequencies are compared in Figures 14–16. As the observing frequency decreases the centroid path becomes larger and more symmetric. As a result, the orbital parameters are more easily determined at radio wavelengths. This implies that simultaneous high-resolution radio and NIR observations of the centroid are capable of identifying black hole spin.

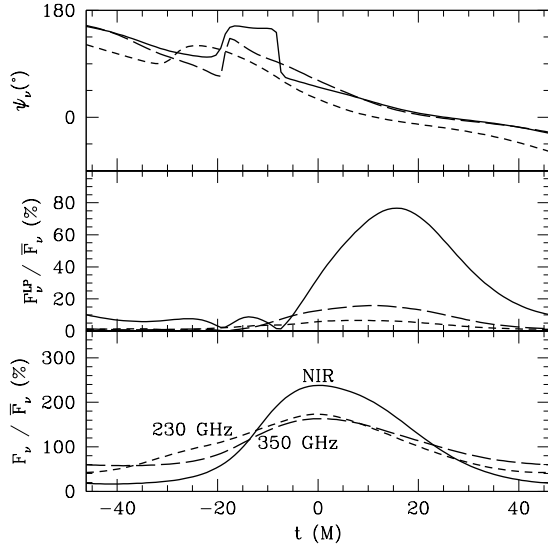


Figure 11. The background subtracted total and polarized flux (bottom and middle panels, respectively) normalized by the average *background subtracted* total flux as functions of time for a spot orbit at $6M$ around a Schwarzschild black hole viewed from 45° above the equatorial plane as observed in the infrared (solid), 350 GHz (long-dash) and 230 GHz (short-dash). The polarization angle, ψ , is shown in the top panel. The time axis is set so that a single orbital period of the $a = 0$ case is shown. For a black hole mass of $4 \times 10^6 M_\odot$ (as in Sgr A*), the time unit is $M = 20$ s.

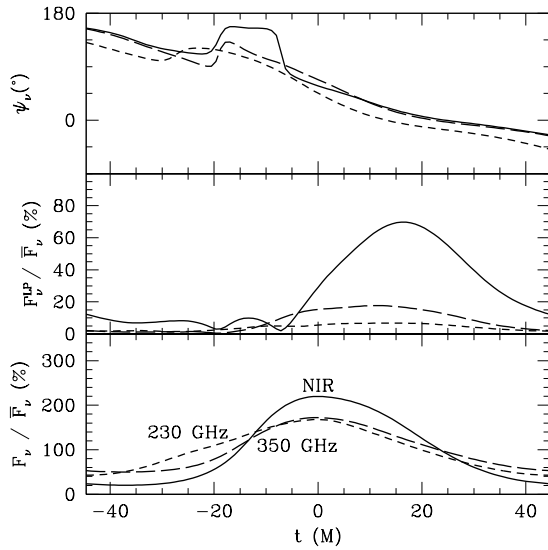


Figure 12. The background subtracted total and polarized flux (bottom and middle panels, respectively) normalized by the average *background subtracted* total flux as functions of time for a spot orbit at $6M$ around a Kerr black hole ($a = 0.5$) viewed from 45° above the equatorial plane as observed in the infrared (solid), 350 GHz (long-dash) and 230 GHz (short-dash). The polarization angle, ψ , is shown in the top panel. The time axis is set so that a single orbital period of the $a = 0$ case is shown. For a black hole mass of $4 \times 10^6 M_\odot$ (as in Sgr A*), the time unit is $M = 20$ s.

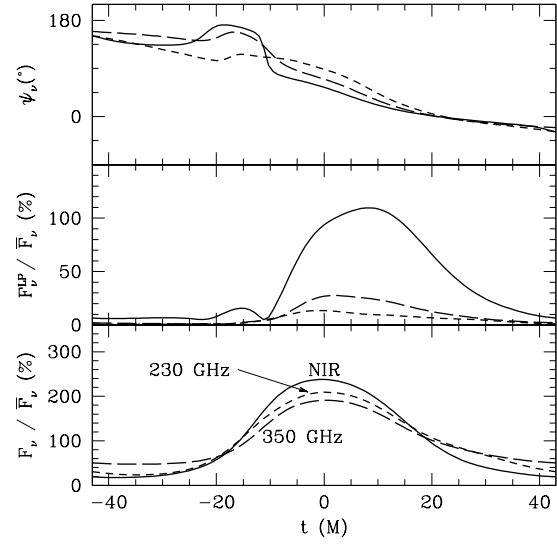


Figure 13. The background subtracted total and polarized flux (bottom and middle panels, respectively) normalized by the average *background subtracted* total flux as functions of time for a spot orbit at $6M$ around a Kerr black hole ($a = 0.998$) viewed from 45° above the equatorial plane as observed in the infrared (solid), 350 GHz (long-dash) and 230 GHz (short-dash). The polarization angle, ψ , is shown in the top panel. The time axis is set so that a single orbital period of the $a = 0$ case is shown. For a black hole mass of $4 \times 10^6 M_\odot$ (as in Sgr A*), the time unit is $M = 20$ s.

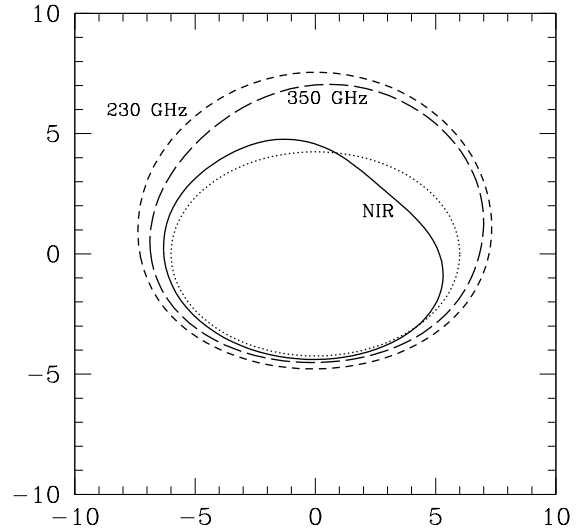


Figure 14. The paths of the background subtracted intensity centroid for circular spot orbits around a Schwarzschild black hole viewed from 45° above the orbital plane at $6M$ as observed in the infrared (solid), 350 GHz (long-dash) and 230 GHz (short-dash). For reference, a circle inclined at 45° is also shown by the dotted lines for each radius. Axes are labeled in units of M (corresponding to an angular scale of roughly $5 \mu\text{as}$ for Sgr A*).

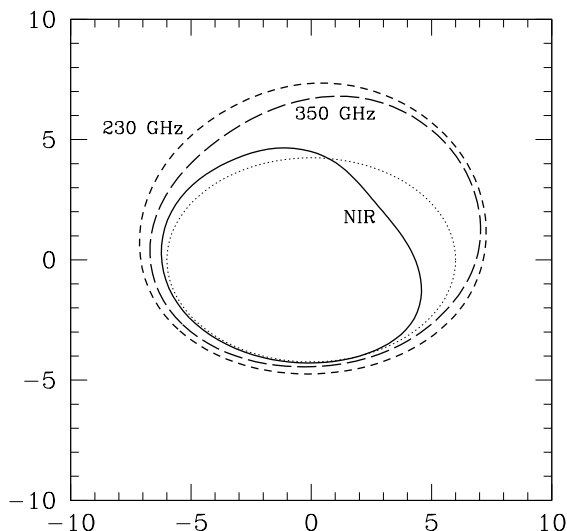


Figure 15. The paths of the background subtracted intensity centroid for circular spot orbits around a Kerr black hole ($a = 0.5$) viewed from 45° above the orbital plane at $6M$ as observed in the infrared (solid), 350 GHz (long-dash) and 230 GHz (short-dash). For reference, a circle inclined at 45° is also shown by the dotted lines for each radius. Axes are labeled in units of M (corresponding to an angular scale of roughly $5 \mu\text{as}$ for Sgr A*).

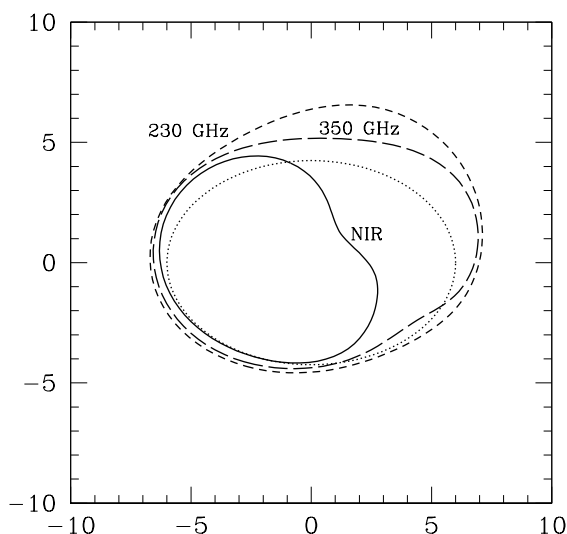


Figure 16. The paths of the background subtracted intensity centroid for circular spot orbits around a Kerr black hole ($a = 0.998$) viewed from 45° above the orbital plane at $6M$ as observed in the infrared (solid), 350 GHz (long-dash) and 230 GHz (short-dash). For reference, a circle inclined at 45° is also shown by the dotted lines for each radius. Axes are labeled in units of M (corresponding to an angular scale of roughly $5 \mu\text{as}$ for Sgr A*).

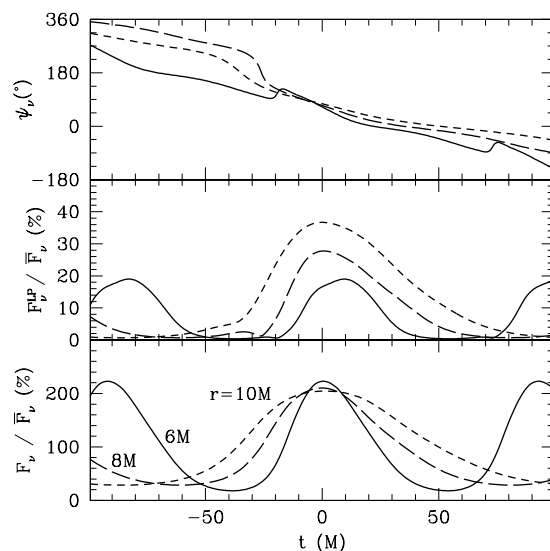


Figure 17. The background subtracted total and polarized flux (bottom and middle panels, respectively) normalized by the average *background subtracted* total flux as functions of time at 350 GHz for spot orbits at $6M$ (solid), $8M$ (long-dash) and $10M$ (short-dash) around a Schwarzschild black hole, viewed from 45° above the equatorial plane. The polarization angle, ψ , is shown in the top panel. The time axis is set so that a single orbital period of the $10M$ case is shown. For a black hole mass of $4 \times 10^6 M_\odot$ (as in Sgr A*), the time unit is $M = 20 \text{ s}$.

5 RADIO

Anticipating high-resolution sub-millimetre observations of the Galactic centre, we present the magnification and polarized flux light curves and image centroids at radio frequencies. As discussed in the previous section, these may be expected to be quantitatively different from those presented in Section 3.

5.1 Light Curves

Figure 17 shows that at 350 GHz the absorption has little effect upon the magnification light curves for moderate orbital inclinations (compare to Figure 2). However, the peak polarized flux is reduced by more than 70% and observed earlier than in the NIR. While the polarization angle continues to exhibit a rapid rotation associated with the development of a secondary image, it is significantly smoothed.

This is especially apparent in Figure 18, which shows the light curves for a number of viewing inclinations, ϑ , (compare to Figure 3). In the case where $\vartheta = 0^\circ$, the emergence of an orthogonal polarization is suppressed, leading to a constant polarization angle. For small ϑ , the peak magnification is also marginally reduced, as may be expected from the larger column density for such viewing angles. Nevertheless, the flare time-scale and peak magnification are still indicative of the orbital radius and inclination. Furthermore, the presence of a flare in the polarized flux is generic.

Figures 19 and 20 show the magnification and polarized flux light curves for various black hole spins as seen at 350 GHz and 230 GHz, respectively (compare to Figure

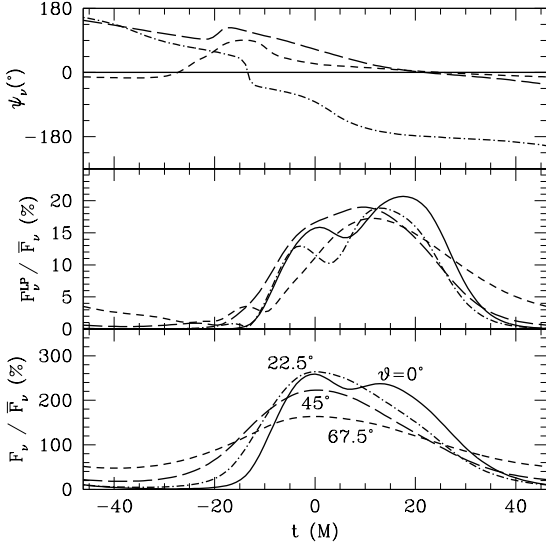


Figure 18. The background subtracted total and polarized flux (bottom and middle panels, respectively) normalized by the average *background subtracted* total flux as functions of time at 350 GHz for a spot orbit at $6M$ around a Schwarzschild black hole viewed from 0° (solid), 22.5° (dash-dot), 45° (long-dash) and 67.5° (short-dash) above the equatorial plane. The polarization angle, ψ , is shown in the top panel. For a black hole mass of $4 \times 10^6 M_\odot$ (as in Sgr A*), the time unit is $M = 20$ s.

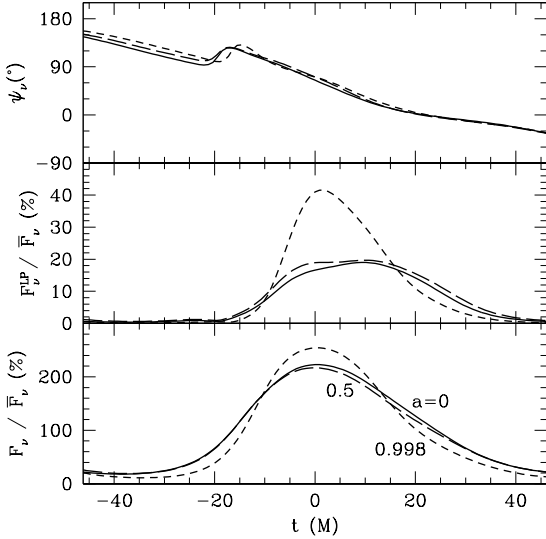


Figure 19. The background subtracted total and polarized flux (bottom and middle panels, respectively) normalized by the average *background subtracted* total flux as functions of time at 350 GHz for a spot orbit at $6M$ around a Kerr black hole with $a = 0$ (solid), $a = 0.5$ (long-dash) and $a = 0.998$ (short-dash) viewed from 45° above the equatorial plane. The polarization angle, ψ , is shown in the top panel. The time axis is set so that a single orbital period of the $a = 0$ case is shown. For a black hole mass of $4 \times 10^6 M_\odot$ (as in Sgr A*), the time unit is $M = 20$ s.

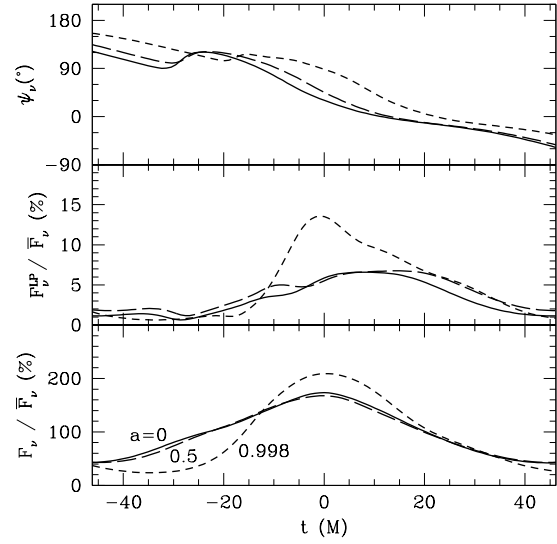


Figure 20. The background subtracted total and polarized flux (bottom and middle panels, respectively) normalized by the average *background subtracted* total flux as functions of time at 230 GHz for a spot orbit at $6M$ around a Kerr black hole with $a = 0$ (solid), $a = 0.5$ (long-dash) and $a = 0.998$ (short-dash) viewed from 45° above the equatorial plane. The polarization angle, ψ , is shown in the top panel. The time axis is set so that a single orbital period of the $a = 0$ case is shown. For a black hole mass of $4 \times 10^6 M_\odot$ (as in Sgr A*), the time unit is $M = 20$ s.

4). Typically, there is little difference among the magnification light curves. However, in both cases the polarized flux clearly discriminates between high and moderate/low black hole spins, varying by roughly a factor of two in both cases. This is likely due to the lower thermal electron density permissible in the high spin model employed (see Table 1).

As in the optically-thin regime described in Section 3.1, the primary difference between high and low spin black holes is likely to be the flaring timescales. Similarly to Figure 5, Figure 21 shows the magnification and polarized flux light curves as functions of *orbital phase*. As in the NIR, the polarization is more sensitive to the black hole spin than the degree of magnification. The opacity associated with the hot-spot orbiting the maximally rotating black hole is significantly larger due primarily to the rapid disk velocity at this position. As a result, this model was significantly more absorbed than the others. Combined with strong gravitational lensing, this effect produces a variation in the flux that is unpolarized and small in comparison with the quiescent disk emission.

5.2 Centroid Paths

Next, we consider the paths of the *background subtracted* image centroids. While in the optically thin regime described in Section 3.2, the disk and hot-spot emission are completely disentangled, in this case the disk opacity can substantially modify the image centroids. In the frequency regime of the optically thick/thin transition, opacity is most significant on the approaching side of the accretion flow, near where the hot-spot is the brightest. This has the effect of reducing the

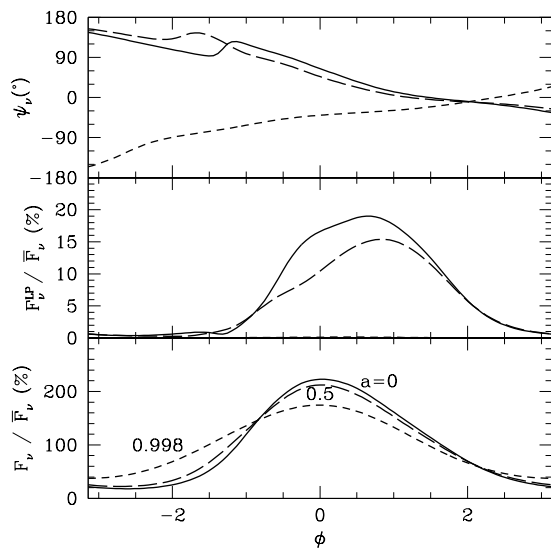


Figure 21. The background subtracted total and polarized flux (bottom and middle panels, respectively) normalized by the average background subtracted total flux as functions of phase at 350 GHz for spot orbits at the prograde ISCO around a Kerr black hole with $a = 0$ (solid), $a = 0.5$ (long-dash) and $a = 0.998$ (short-dash) viewed from 45° above the equatorial plane. The polarization angle, ψ , is shown in the top panel. The time axis is set so that a single orbital period of the $a = 0$ case is shown. For a black hole mass of $4 \times 10^6 M_\odot$ (as in Sgr A*), the time unit is $M = 20$ s.

brightness contrast between the approaching and receding portions of the hot-spot orbit. Since the brightest regions dominate the location of the image centroid, this has significant implications for the centroid paths.

Figure 22 shows the centroid paths for hot-spots orbiting at three radii, viewed from 45° above the orbital plane. This is similar to Figure 12 in Broderick & Loeb (2005b), primarily due to the reduced brightness contrast mentioned above. The orbits are noticeably larger than those in Figure 6, though the major axis distance is similar.

Various viewing inclinations are shown in Figure 23 (cf., Figure 7). As in Figure 22, the centroid paths are larger than those found in the NIR. For low ϑ , this substantially modifies the shape of the centroid path. Nonetheless, the nearest region of the orbit (bottom) is close to the unlensed orbit positions (shown by the dotted lines), and thus the semi-minor axis is still diagnostic of the orbital inclination.

Figures 24 and 25 show the centroid paths for various black hole spins as viewed at 350 GHz and 230 GHz, respectively (cf., Figure 8). In all cases the paths are larger than in the NIR and, unlike the NIR, are larger than expected in the absence of gravitational and opacity effects (shown by the dotted line). In all cases, the semi-minor axis again appears to be a good measure of the orbital inclination.

The centroid paths for orbits at the ISCO of the three black hole spins we considered are shown in Figure 26. As in the NIR, the inner orbits are substantially modified by strong lensing, and in this case, opacity. However, as mentioned previously, the flux variation associated with the

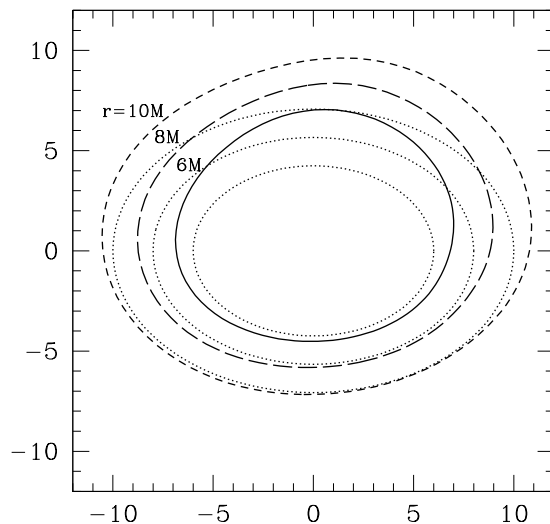


Figure 22. The paths of the background subtracted intensity centroid at 350 GHz for circular spot orbits around a Schwarzschild black hole viewed from 45° above the orbital plane with radii $6M$ (solid), $8M$ (long-dash) and $10M$ (short dash). For reference, a circle inclined at 45° is also shown by the dotted lines for each radius. Axes are labeled in units of M (corresponding to an angular scale of roughly $5 \mu\text{as}$ for Sgr A*).

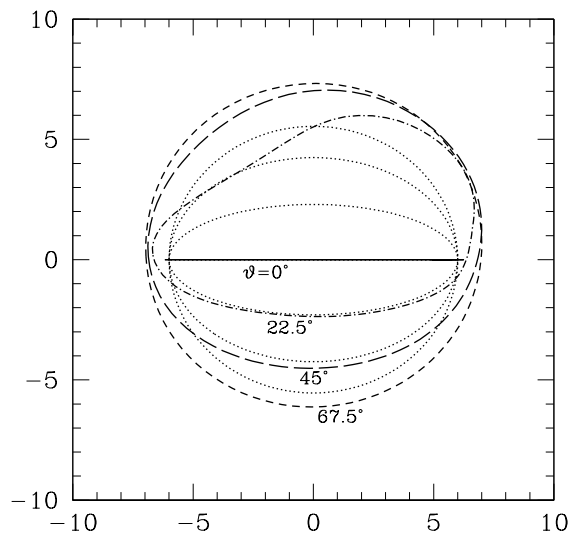


Figure 23. The paths of the background subtracted intensity centroid at 350 GHz for circular spot orbits around a Schwarzschild black hole with radius $6M$ viewed from 0° (solid), 22.5° (dash-dot), 45° (long-dash) and 67.5° (short-dash) above the orbital plane. For reference, a circles inclined at each angle are shown by the dotted lines. Axes are labeled in units of M (corresponding to an angular scale of roughly $5 \mu\text{as}$ for Sgr A*).

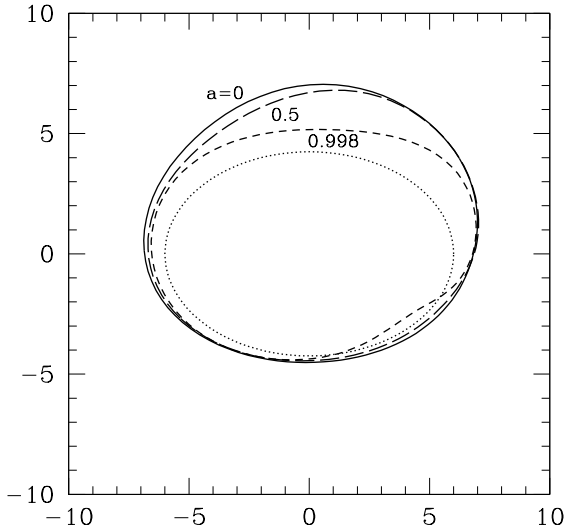


Figure 24. The paths of the background subtracted intensity centroid at 350 GHz for circular spot orbits with radius $6M$ in the equatorial plane around a Kerr black hole viewed from 45° above the orbital plane for $a = 0$ (solid), $a = 0.5$ (long-dash) and $a = 0.998$ (short-dash). For reference, a circle inclined at 45° is also shown by the dotted line. Axes are labeled in units of M (corresponding to an angular scale of roughly $5 \mu\text{as}$ for Sgr A*).

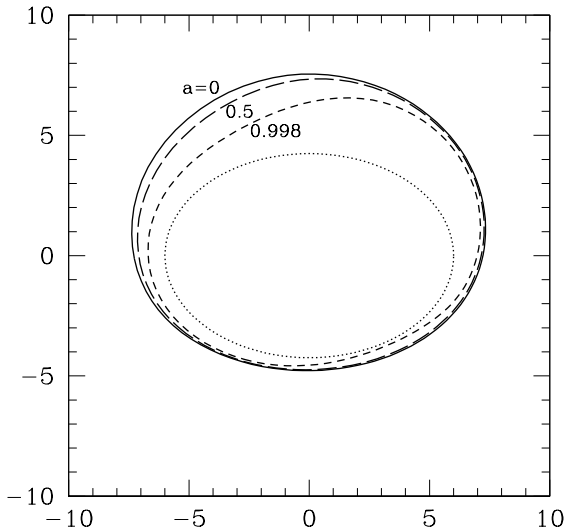


Figure 25. The paths of the background subtracted intensity centroid at 230 GHz for circular spot orbits with radius $6M$ in the equatorial plane around a Kerr black hole viewed from 45° above the orbital plane for $a = 0$ (solid), $a = 0.5$ (long-dash) and $a = 0.998$ (short-dash). For reference, a circle inclined at 45° is also shown by the dotted line. Axes are labeled in units of M (corresponding to an angular scale of roughly $5 \mu\text{as}$ for Sgr A*).

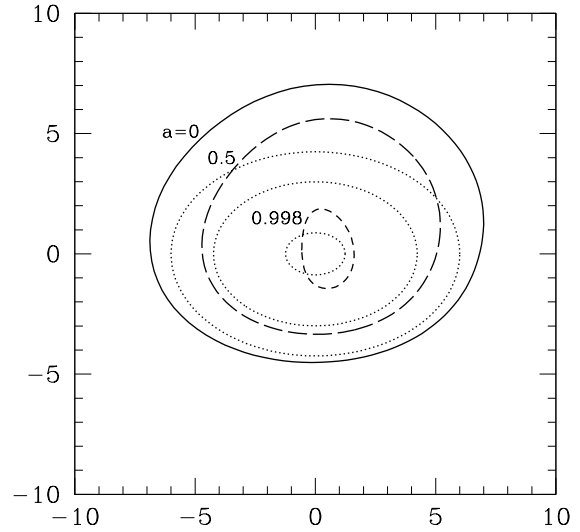


Figure 26. The paths of the background subtracted intensity centroid at 350 GHz for circular spot orbits around a Kerr black hole viewed from 45° above the orbital plane at the prograde ISCO for $a = 0$ (solid), $a = 0.5$ (long-dash) and $a = 0.998$ (short-dash). For reference, a circle inclined at 45° is also shown by the dotted lines for spin. Axes are labeled in units of M (corresponding to an angular scale of roughly $5 \mu\text{as}$ for Sgr A*).

high-spin case is small, and thus it is not clear that the centroid path will be measurable in this case.

6 CONCLUSIONS

The photon trapping radius of the black hole in the center of the Milky-Way galaxy has the largest apparent sizes among all known black holes, occupying an angular scale of tens of micro-arcseconds on the sky. This scale will be within reach of forthcoming observatories, such as a sub-millimetre VLBA (for imaging), or the PRIMA instrument on the VLT (for monitoring shifts in the infrared image centroid during flares). Imaging hot spots in the immediate vicinity of an accreting black hole provides a new method for testing general relativity and measuring the black hole mass and spin.

The image and centroid shifts of a compact population of non-thermal electrons may be used to constrain the mass and spin of the central black hole. At radio wavelengths such a spot would persist for many orbitally periods, ultimately being sheared into a ring, while in the NIR such a spot would cool rapidly, surviving approximately a single orbit.

At the sub-millimetre frequencies currently proposed for the VLBA imaging of the Galactic centre, the opacity of the underlying steady accretion flow has a significant effect upon the images and centroid motions. Nonetheless, it remains possible to extract the black hole mass and spin from these. Furthermore, combined with the NIR data (at which the accretion flow opacity is negligible) this will provide a method by which the accretion flow may be isolated.

While polarization is significant in both the radio and NIR regimes, the enhanced opacity at radio wavelengths reduces the polarization signatures of strong lensing that

are most noticeable for the polarization angle and polarized flux in the NIR. Immediately prior to maximum magnification, rapid changes in the orientation of the polarization take place in the NIR. These are systematically smoothed in the radio, though the polarization does rotate as expected for a toroidal magnetic field.

We have used simple models for the underlying accretion flow and the hot spot. Future work can improve upon our results using three-dimensional, fully relativistic, magneto-hydrodynamic simulations of the accretion flow, in which hot spots (or flares) arise naturally as magnetic reconnection events and/or at shocks.

ACKNOWLEDGMENTS

This work was supported in part by NASA grant NAG 5-13292 and NNG05GH54G (for A.L.). A.E.B. gratefully acknowledges the support of an ITC Fellowship from Harvard College Observatory.

REFERENCES

- Baganoff F. K., Bautz M. W., Brandt W. N., Chartas G., Feigelson E. D., Garmire G. P., Maeda Y., Morris M., Ricker G. R., Townsley L. K., Walter F., 2001, *Nature*, 413, 45
- Broderick A., Blandford R., 2003, *MNRAS*, 342, 1280
- Broderick A., Blandford R., 2004, *MNRAS*, 349, 994
- Broderick A. E., 2005, *MNRAS*, submitted
- Broderick A. E., Loeb A., 2005a, *ApJL*, submitted (astro-ph/0508386)
- Broderick A. E., Loeb A., 2005b, *MNRAS*, in press (astro-ph/0506433)
- Connors P. A., Stark R. F., Piran T., 1980, *ApJ*, 235, 224
- De Villiers J., Hawley J. F., Krolik J. H., 2003, *ApJ*, 599, 1238
- Doeleman S., Bower G., 2004, *Galactic Center Newsletter*, 18, 6
- Eckart A., Baganoff F. K., Morris M., Bautz M. W., Brandt W. N., Garmire G. P., Genzel R., Ott T., Ricker G. R., Straubmeier C., Viehmann T., Schödel R., Bower G. C., Goldston J. E., 2004, *A&A*, 427, 1
- Falcke H., Melia F., Agol E., 2000, *ApJL*, 528, L13
- Genzel R., Schödel R., Ott T., Eckart A., Alexander T., Lacombe F., Rouan D., Aschenbach B., 2003, *Nature*, 425, 934
- Ghez A. M., Wright S. A., Matthews K., Thompson D., Le Mignant D., Tanner A., Hornstein S. D., Morris M., Becklin E. E., Soifer B. T., 2004, *ApJL*, 601, L159
- Goldwurm A., Brion E., Goldoni P., Ferrando P., Daigne F., Decourchelle A., Warwick R. S., Predehl P., 2003, *ApJ*, 584, 751
- Jones T. W., O'Dell S. L., 1977, *ApJ*, 214, 522
- Laor A., Netzer H., Piran T., 1990, *MNRAS*, 242, 560
- Lindquist R. W., 1966, *Anal. of Physics*, 37, 487
- Miyoshi M., Ishitsuka J. K., Kamenno S., Shen Z., Horiuchi S., 2004, *Progress of Theoretical Physics Supplement*, 155, 186
- Paumard T., Perrin G., Eckart A., Genzel R., Léna P., Schödel R., Eisenhauer F., Müller T., Gillessen S., 2005

"ESO Astrophysics Symposia", "Scientific prospects for VLTI in the galactic centre: Getting to the schwarzschild radius" *in press*

Takahashi R., 2004, *ApJ*, 611, 996

Takahashi R., 2005, *Publ. Astron. Soc. Japan*, 57, 273

Yuan F., Quataert E., Narayan R., 2003, *ApJ*, 598, 301

Yuan F., Quataert E., Narayan R., 2004, *ApJ*, 606, 894

This paper has been typeset from a \TeX / \LaTeX file prepared by the author.